Materials and Design 162 (2019) 394–404

Contents lists available at ScienceDirect

Materials and Design

journal homepage: www.elsevier.com/locate/matdes

Continuous graded Gyroid cellular structures fabricated by selective laser melting: Design, manufacturing and mechanical properties

Lei Yang [a,b], Raya Mertens [b], Massimiliano Ferrucci [b], Chunze Yan [a,*], Yusheng Shi [a], Shoufeng Yang [b,c,**]

[a] State Key Laboratory of Materials Processing and Die & Mould Technology, School of Materials Science and Engineering, Huazhong University of Science and Technology, Wuhan 430074, China
[b] Department of Mechanical Engineering, Member of Flanders Make, KU Leuven (Catholic University of Leuven), 3001 Leuven, Belgium
[c] Materials Research Group, Faculty of Engineering and the Environment, University of Southampton, Southampton SO17 1BJ, UK

HIGHLIGHTS

- Continuous graded Gyroid cellular structures (GCSs) were fabricated by SLM.
- Novel deformation and mechanical properties were gained compared to uniform cellular.
- The effect of gradient direction was investigated for GCSs.
- Novel sub-layer collapses are founded in GCSs with gradient along building direction.
- Mathematical models were developed to calculate Young's modulus and strength of GCSs.

GRAPHICAL ABSTRACT

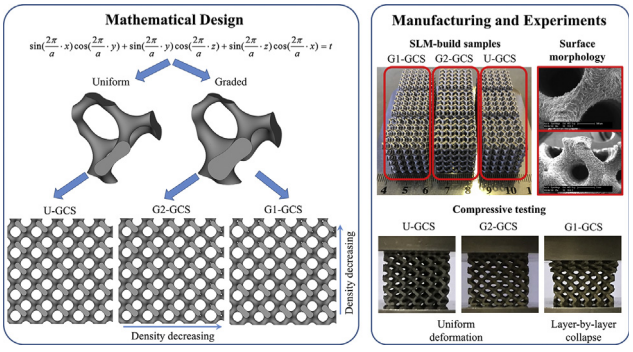

ARTICLE INFO

Article history:
Received 17 October 2018
Received in revised form 21 November 2018
Accepted 3 December 2018
Available online 06 December 2018

Keywords:
Graded cellular structure
Selective laser melting
Energy absorption
Compressive response
Triply periodic minimal surface

ABSTRACT

Functional graded cellular materials (FGCMs) have attracted increasing attentions for their improved properties when compared to uniform cellular structures. In this work, graded Gyroid cellular structures (GCSs) with varying gradient directions were designed and manufactured via selective laser melting (SLM). As a reference, uniform structures were also manufactured. The surface morphology and mechanical response of these structures under compressive loads were investigated. Results indicate high manufacturability and repeatability of GCSs manufactured by SLM. Optimized density distribution gives these structures novel deformation and mechanical properties. GCSs with density gradient perpendicular to the loading direction exhibit deformation behaviours similar to uniform ones, while GCSs with the gradient parallel to the loading direction exhibit layer-by-layer deformation and collapse behaviour. A novel phenomenon of sub-layer collapses is found in GCSs with gradient parallel to the loading direction. Furthermore, mathematical models were developed to predict and customize the mechanical properties of graded cellular structures by optimizing the relative density of each layer. These significant findings illustrate that graded cellular structures have high application prospect in various industries, particularly given the fact that additive manufacturing has been an enabler of cellular structure fabrication.

* Correspondence to: C. Yan, School of Materials Science and Engineering, Huazhong University of Science and Technology, Wuhan 430074, China.
** Correspondence to: S. Yang, Department of Mechanical Engineering, Member of Flanders Make, KU Leuven (Catholic University of Leuven), 3001 Leuven, Belgium.
E-mail addresses: c_yan@hust.edu.cn (C. Yan), shoufeng.yang@kuleuven.be (S. Yang).

https://doi.org/10.1016/j.matdes.2018.12.007

Nomenclature

a	The unit cell size of Gyroid cellular structure
t	The parameter controls the volume surrounded by the Gyroid surface
ρ_{cel}	Density of the cellular structure
ρ_m	Density of the matrix material
ρ^*	Relative density of the cellular structure
E_{cel}	Young's Modulus of the cellular structure
E_m	Young's Modulus of the matrix material
E^*	Relative Modulus of the cellular structure
$\sigma_{cel.\ pl}$	Plateau stress of the cellular structure
σ_m	Yield stress of the matrix material
σ^*	Relative strength of the cellular structure
ε_{cd}	Onset strain of densification
$\eta(\varepsilon)$	Energy absorption efficiency
W_v	Energy absorption per volume
m, n, α	Coefficients in Gibson-Ashby equations
j	the layer number of Graded cellular structure in equations
k_j	The percentage of different layer in the graded cellular structure
E_j	Young's modulus of different layer in the graded cellular structure
σ_j	Yield stress of different layer in the graded cellular structure

1. Introduction

Functional graded cellular materials (FGCMs) based on optimized distributions of pore size, pore morphology, and relative density (RD) have attracted increasing attention for their outperformed properties including the combination of high porosity, adequate strength, excellent high energy absorption, optimized in-growth of tissues, and the ability to withstand varying mechanical stress at specific regions [1–3]. All these characteristics make FGCMs promising for the applications of lightweight, orthopedics, acoustics, aerospace, and automotive industries [4–6]. For instance, Li et al. [1] investigated graded mesh structures and found that the graded mesh absorbed more energy than their non-graded counterparts. Maskery et al. [7] achieved high energy absorption capability through designing graded lattice structures with continuously changing density along the structure layers.

Conventional processing techniques available for the fabrication of cellular structures mainly include melt gas injection [8], investment casting [9], polymeric sponge replication [10], physical vapor deposition [11], and sheet metal technique [12]. However, these conventional techniques do not permit the realization of complex cellular structures with highly controllable RD, pore geometry, and pore size and distribution. The most commonly used methods to precisely fabricate FGCMs are additive manufacturing (AM) technologies, based on the layer-by-layer addition of material at the micro level. AM technologies, such as selective laser melting (SLM) [13–17], electron beam melting (EBM) [18–20], enables the fabrication of complex structures with high resolutions, providing complete control of both the RD and geometric features.

To date, FGCMs designed in previous work mostly possess strut-based unit cells which are derived by Boolean operation of geometric primitives [7,15,17]. However, these strut-based geometries lower the manufacturability, which has been confirmed by the experiments [21]. Moreover, these cellular structures can experience severe stress concentrations on the abrupt turning under loading and result in early fracture near the joints of struts [21,22].

Triply periodic minimal surfaces (TPMSs) are minimal surfaces with mean curvature of zero and periodic structures in three coordinate directions [23]. TPMS structures have already been shown to be a versatile source of biomorphic scaffold designs and possess high manufacturability in the AM process and uniform stress distribution under loading, due to its geometrical characteristics [24–26]. Thus, TPMSs are considered as the most promising biomaterial structures [27–31]. The Gyroid surface is a type of TPMS and was first discovered in 1967 by Luzzati et al. [32,33]. In recent years, much attention has been paid on the Gyroid cellular structure (GCS). The manufacturability, surface morphology, microstructure, mechanical response, orientation dependence and chemical etching of uniform GCSs have been systematically investigated in our previous works [24,25,34–37]. However, to the best of our knowledge, limited literature has been published to design and investigate the graded Gyroid cellular structure (G-GCS).

Therefore, in this paper, continuous G-GCSs with the RD changing from 20% to 10% and the rotated G-GCSs were designed and manufactured by SLM. The uniform GCS counterparts with the RD of 15% were also fabricated. Compressive tests were performed to assess the mechanical responses and energy absorption capacity of the samples. Furthermore, Gibson-Ashby models for cellular structures were applied to determine the pre-factor coefficients. Iso-stress composite model and Kelvin-Voigt model were introduced to predict the mechanical responses of G-GCSs using the mechanical properties of uniform GCS gained by the Gibson-Ashby equations.

1.1. The Gibson-Ashby model of cellular structures

In this work, the effect of RD on the mechanical properties, such as Young's modulus, plateau stress, and onset strain of densification was described through Gibson–Ashby equations [38] as follows,

$$\frac{E_{cel}}{E_m} = C_1\left(\frac{\rho_{cel}}{\rho_m}\right)^m \tag{1}$$

$$\frac{\sigma_{cel.pl}}{\sigma_m} = C_2\left(\frac{\rho_{cel}}{\rho_m}\right)^n \tag{2}$$

$$\varepsilon_{cd} = 1-\alpha\left(\frac{\rho_{cel}}{\rho_m}\right) \tag{3}$$

where the values of coefficients C_1 and C_2 are within the ranges of 0.1–4.0, and 0.25–0.35, respectively. The m and n are constants with values of approximately 2 and ~3/2, respectively, and α varies correspondingly to the matrix material deformation behaviour: approximately 10/3 and 2 for elastomeric and plastic foams, respectively [38,39].

Uniform density cellular structures exhibit three ideal regimes under compressive testing [38]: a linear elastic regime, followed by a plateau regime with approximately constant stress, and a final densification regime with steeply increasing stress. The linear elastic regime is driven by the bending for the inclined cell walls/struts or by the stretching for the vertical cell walls/struts and characterized by Young's modulus, E_{cel}. The plateau regime can be ascribed to the creation of plastic hinges at the sections or joints of the cellular struts. Since the matrix material exhibits plastic yielding, the plateau regime will be a long plateau, as opposed to a fluctuation around a stress value exhibited by brittle materials. Finally, the structure will enter the densification regime starting from a strain ε_{cd}, where the individual cell walls or struts come into contact with each other and exhibits dramatically increased strength.

The plateau stress $\sigma_{cel.\ pl}$ is defined as the arithmetical mean of the stresses at strain intervals between 20% and 30% or between 20% and 40% compressive strain, according to ISO 13314: 2011 [40]. The value ε_{cd} is identified using the energy efficiency method outlined by

[39,41]. Based on the uniaxial stress-strain curve of the cellular material, the energy absorption efficiency can be defined by

$$\eta(\varepsilon) = \frac{1}{\sigma(\varepsilon)} \int_0^{\varepsilon} \sigma(\varepsilon) d\varepsilon \tag{4}$$

The onset of densification determined by the energy absorption efficiency is given by

$$\left. \frac{d\eta(\varepsilon)}{d\varepsilon} \right|_{\varepsilon=\varepsilon_{cd}} = 0 \tag{5}$$

for which the energy absorption efficiency reaches a maximum on the efficiency-strain curve. The energy absorption capacity of cellular structures is determined using numerical integration, giving the area under the compressive stress-strain curves [15]:

$$W_v = \int_0^{\varepsilon} \sigma(\varepsilon) d\varepsilon \tag{6}$$

2. Experimental methodology

2.1. Modelling of GCSs

MATLAB (Mathworks Inc., USA) software was utilized to design the Gyroid unit cell. As shown in Fig. 1(a), a Gyroid unit cell was generated by mathematical equations.

$$\sin\left(\frac{2\pi}{a}\cdot x\right)\cos\left(\frac{2\pi}{a}\cdot y\right) + \sin\left(\frac{2\pi}{a}\cdot y\right)\cos\left(\frac{2\pi}{a}\cdot z\right) + \sin\left(\frac{2\pi}{a}\cdot z\right)\cos\left(\frac{2\pi}{a}\cdot x\right) = t, \tag{7}$$

where a is the unit cell size, and parameter t controls the volume surrounded by the Gyroid surface. There is a nearly linear relationship between RD of the unit cell and parameter t, as discussed by Scherer et al. [42]. To generate graded Gyroid unit cell, the controlling parameter t varies continuously with z position, resulting in a continuously changing RD. As shown in Fig. 1(b), a graded Gyroid unit cell with RD changing from 20% to 5% was designed and presented here. Fig. 1(c) and (d) are front views of uniform and graded Gyroid unit cells, respectively. Fig. 1(c) shows 4 equivalent sub-layers in one uniform unit cell along z direction, while Fig. 1(d) shows 4 gradient sub-layers.

Each Gyroid unit cell in the uniform Gyroid cellular structures (U-GCSs) is 4 mm × 4 mm × 4 mm in size. An entire U-GCS consists of five unit cells duplicated along each coordinate direction (X, Y, Z), resulting in a total structure size of 20 mm × 20 mm × 20 mm with 15% RD (Fig. 2a). Continuous graded Gyroid cellular structures (G-GCSs) with density gradient along the building direction (denoted as G1-GCS) were designed with density decrease continuously and gradually from 20% (bottom layer) to 10% (top layer) throughout the structure layers with the same unit cell size 4 mm. The continuous change ensures smooth density transitions at the boundaries of the lattice structure layers, as shown in Fig. 2(b). To investigate the mechanical responses of graded Gyroid cellular structures along different loading direction, the model in Fig. 2(b) was rotated by 90° with respect to x axial (i.e. the density gradient is perpendicular to the build and loading directions) and named G2-GCS with the RD changing along Y, as shown in Fig. 2(c). For each structure (U-GCS, G1-GCS, and G2-GCS), three samples were additively manufactured per the process described in Section 2.2.

2.2. Manufacturing of GCSs

Designed cellular structures were manufactured on an M-lab cusing instrument (Concept Laser GmbH, Germany) with a 100 W fibre laser. A

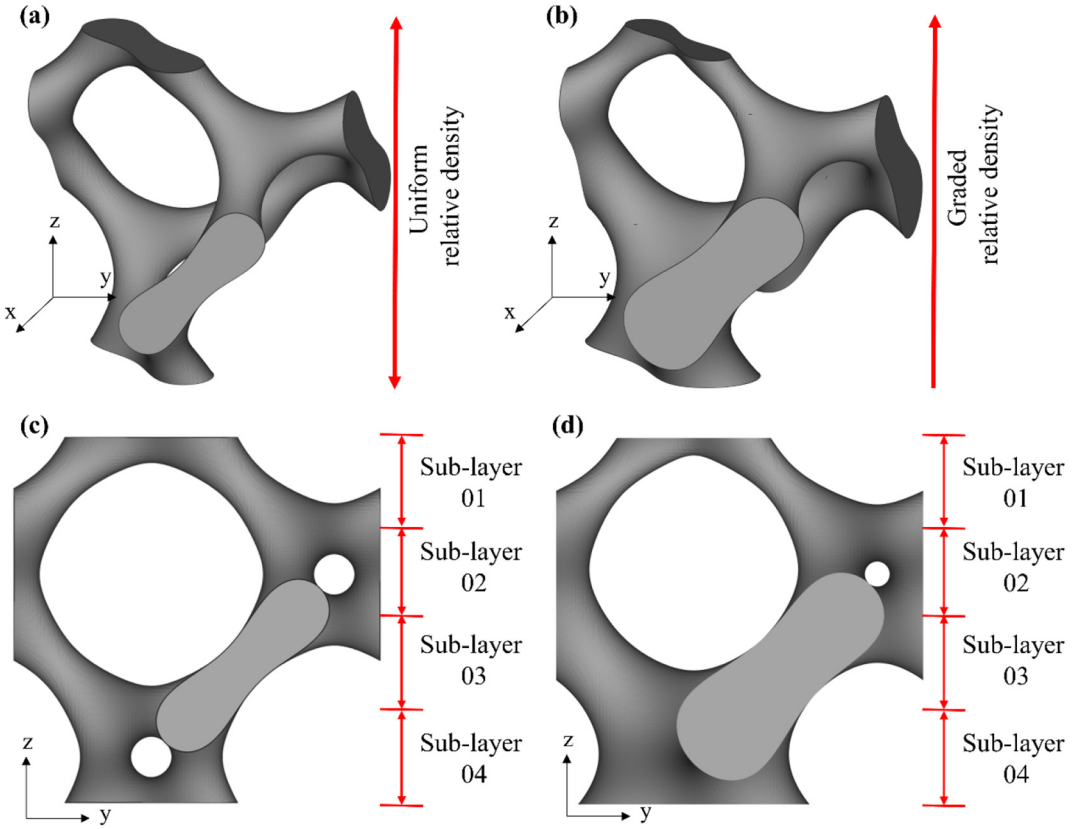

Fig. 1. Gyroid unit cells: (a) uniform unit cell, (b) continuous graded Gyroid unit cell (RD decrease from 20% to 5% with increasing z position), (c) and (d) front views of uniform and graded Gyroid unit cells.

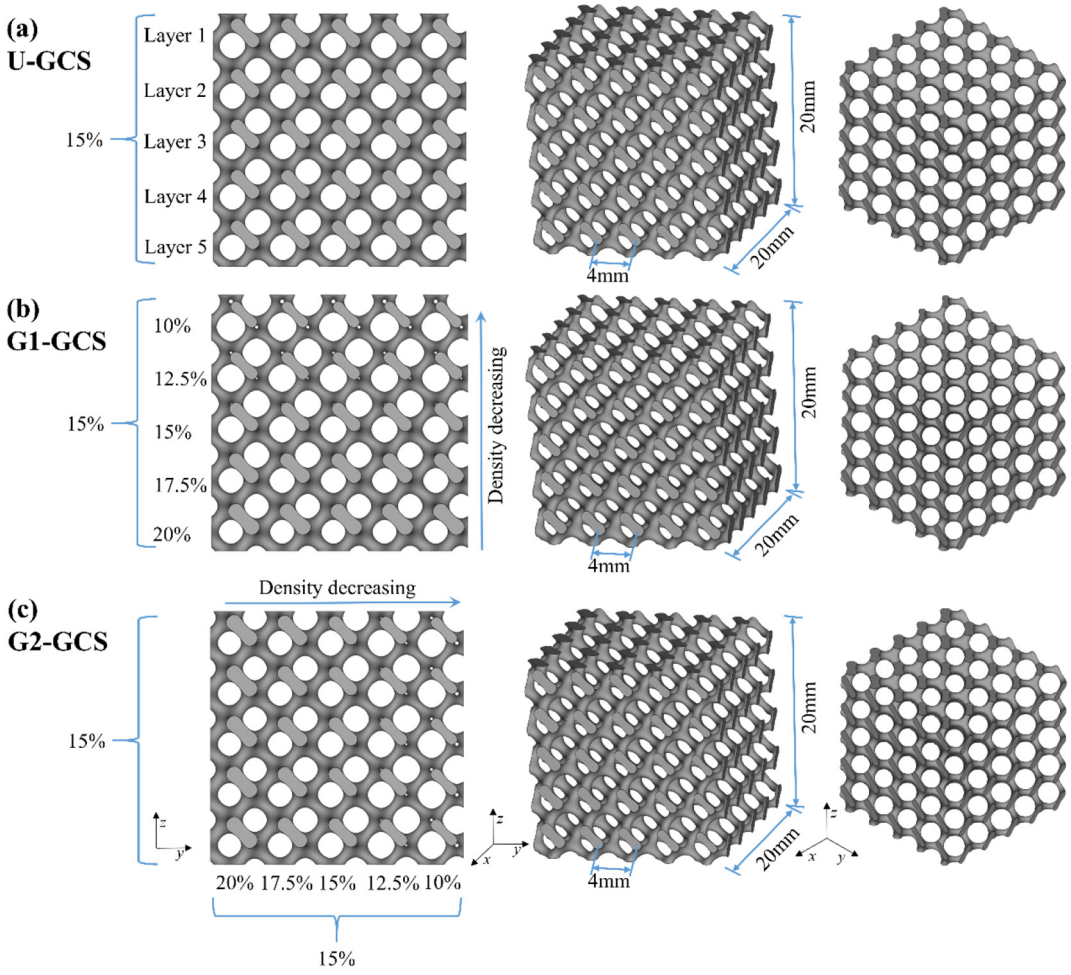

Fig. 2. The CAD models of (a) uniform Gyroid unit cell, (b) continuous Gyroid with the gradient along z direction, and (c) continuous Gyroid with the gradient along y direction.

316 L powder with Gaussian distribution was purchased from Praxair Surface Technologies, Inc. Based on an initial parameter optimization, the optimized processing parameters for the 316 L powder are: laser power of 90 W, hatch spacing of 0.077 mm, scanning speed of 600 mm/s, and layer thickness of 30 μm. All parts were built using a bi-directional scanning strategy after contour scanning. This pattern was rotated over 90° between layers. The SLM process was performed in an inert atmosphere, using argon as the protective gas. Completed samples were removed from the base plate via wire electrical discharge machining (Wire-EDM) and ultrasonically cleaned in pure ethyl alcohol to remove trapped powder particles. Air jet cleaning was utilized to dry the wet samples and ensure that all contaminations (including loose powder) had been removed. The as-built samples before Wire-EDM are presented in Fig. 3.

2.3. Measurements and characterization

Surface morphology prior to the deformation was studied using scanning electron microscope Philips XL 30 FEG. Uniaxial compression tests were performed on the uniform and graded cellular structures with an Instron 5985 instrument equipped with a 100 kN load cell. Cellular structures were centrally placed between two steel plates (65 mm diameter × 10 mm thickness). The bottom plate was fixed, while the top one was displaced at a constant speed of 0.02 mm/s downwards, i.e. 0.1% strain rate of the entire cellular structure in accordance with ISO 13314: 2011 [40]. To avoid the effects of build orientation [43], all compression tests were conducted along the build direction (Z). The applied loads were obtained to determine the compressive stress through dividing the load value by the effective area of the lattice structures. A high-speed camera was employed during the compressive tests to capture and record all deformation stages of the as-built cellular structures.

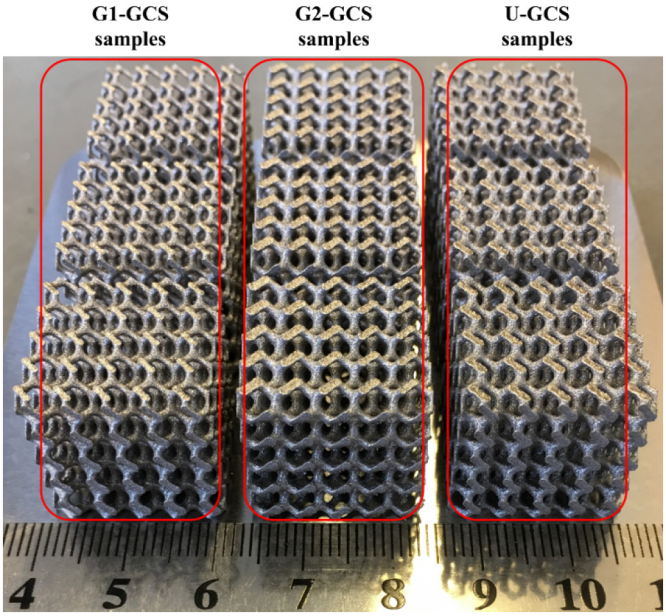

Fig. 3. The fabricated Gyroid cellular structures.

2.4. Finite element method

To investigate the effect of gradient on stress distribution as well as dynamic deformation of GCS, Finite element (FE) analysis was used to simulate the compressive process of GCS with commercial software, DEFORM-3D [44]. SLM-made parts are believed to have certain amount of error compared with the designed model due to the nature of SLM process [45,46]. Also, the mechanical properties of SLM-made materials also show significant differences from casted or forged materials [47]. Therefore, hypotheses are made in this FE model to simplify the material model. The first hypothesis is that the SLM-made structures are consistent with the designed CAD. The second hypothesis is that the material property of the SLM-built 316 L is still the same as the materials tested through standard tensile samples. The aim of FE simulation is to qualitatively analyze the deformation process and the stress distribution; therefore, these two hypotheses are reasonable. The material was assumed to have an elastic modulus of 210 GPa and a Poisson's ratio of 0.3 [48]. A plastic flow model with isotropic hardening in the material library of DEFORM-3D was obtained. The 3D solid element of the 4-node tetrahedral type was employed to mesh the lattice models with six degrees of freedom per node in this simulation process.

3. Results and discussion

3.1. Surface morphologies of the as-built GCSs

Fig. 4 shows the SEM images of G1-GCS sample together with the engineering design. The SLM-fabricated GCS sample agrees well with the designed model, presenting circular struts and spherical pores. By comparing strut images of various layers, as shown in Fig. 4(a) and (b), it can be found that the G-GCS can be successfully manufactured by SLM technology with variable RD in different layers. It is also observed that the SLM-made GCS exhibits rough surfaces, due to partially melted powders boned on the surfaces of GCS and the stair-stepping effect as shown in Fig. 4(c).

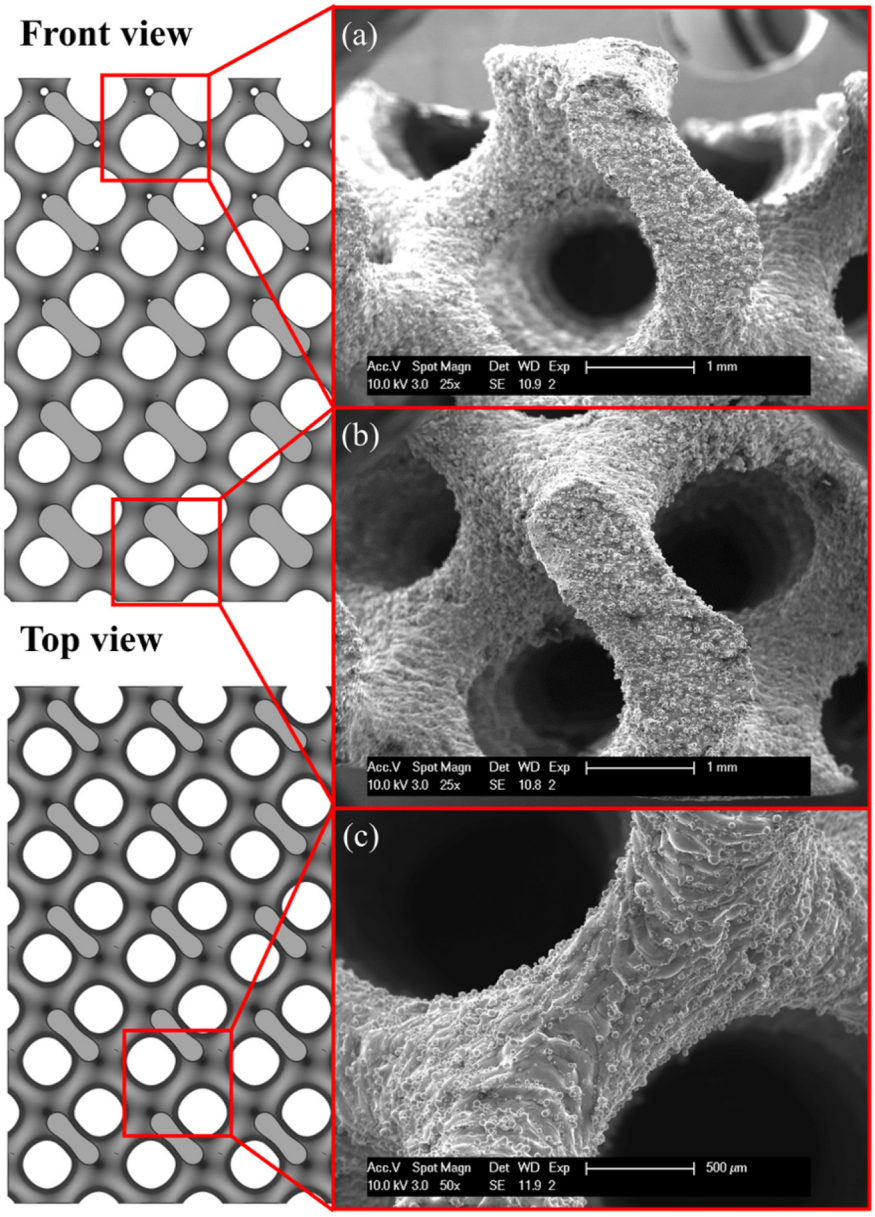

Fig. 4. SEM images of SLM-fabricated G1-GCS: (a) and (b) the front view showing layer-by-layer variable RD and (c) the top view of a strut.

3.2. Mechanical responses of GCSs under compressive testing

In this section, the mechanical response of GCSs to compression testing is evaluated by analysing the deformation characteristics and collapses of GCSs as well as calculating the mechanical properties under compressive testing.

3.2.1. Deformation and collapses stages of GCSs

Fig. 5(a) shows the deformation stages of U-GCS and G2-GCS at several levels of overall strain: 0%, 15%, 30%, 45%, and 60% and Fig. 5 (b) shows layer-by-layer collapses of G1-GCS recorded on a high-speed camera. Fig. 6 shows the experimental stress-strain curves of GCSs under compressive testing. Fig. 7(a) illustrates the stress distribution of GCSs at 2% overall strain under compressive testing, while Fig. 7 (b) presents the deformation of points in each layer of GCSs versus overall strain. The position of chosen points is shown in Fig. 7(a).

As shown in Fig. 5(a), deformation behaviours of U-GCS and G2-GCS were quite similar, due to the uniform-density along the loading direction. In the primary stage, the bottom layers of both U-GCS and G2-GCS firstly deform due to the uncomplete unit cells caused by EDM process. Then, the compressive deformation across the z-y plane is fairly uniform, as shown by arrows in Fig. 5(a), despite the density gradient perpendicular to the loading direction for G2-GCS. The curves of U-GCS and G2-GCS in Fig. 6 exhibit three ideal regimes under compressive testing, just as Gibson and Ashby described in [38]: a linear elastic regime, a plateau regime, and a densification regime. The stress distribution in Fig. 7 (a) illustrate that the stress level for U-GCS is almost uniform in the whole model, while for G2-GCS, the stress concentrates at the unit cells with high RD and unit cells with the same RD in different layers still experience equivalent stress. The displacement figures in Fig. 7 (b) show that points in G2-GCS experience the same uniform deformation process with points in U-GCS. The results demonstrate that the density gradient perpendicular to the loading direction does not affect the deformation characteristic of cellular structures.

Camera images in Fig. 5(b) and stress-strain curves in Fig. 6 indicate that cellular structures with a gradient along the building direction exhibit distinct deformation defined by a layer-by-layer collapse, starting with the lowest density layer and in consequence with increasing RD, as shown by arrows in Fig. 5(b). Collapse layers are identified next to

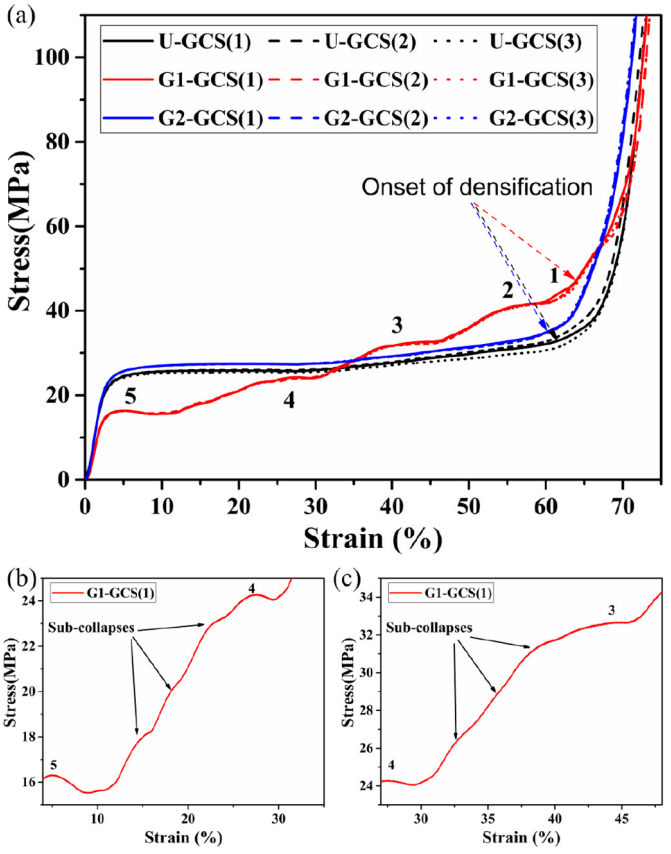

Fig. 6. Compressive stress-strain curves of GCSs. Notations (1), (2), and (3) in the legend correspond to three samples of the same type of GCS. Numbers 5, 4, 3, 2, and 1 in the plot indicate the collapse of cellular layers of G1-GCS.

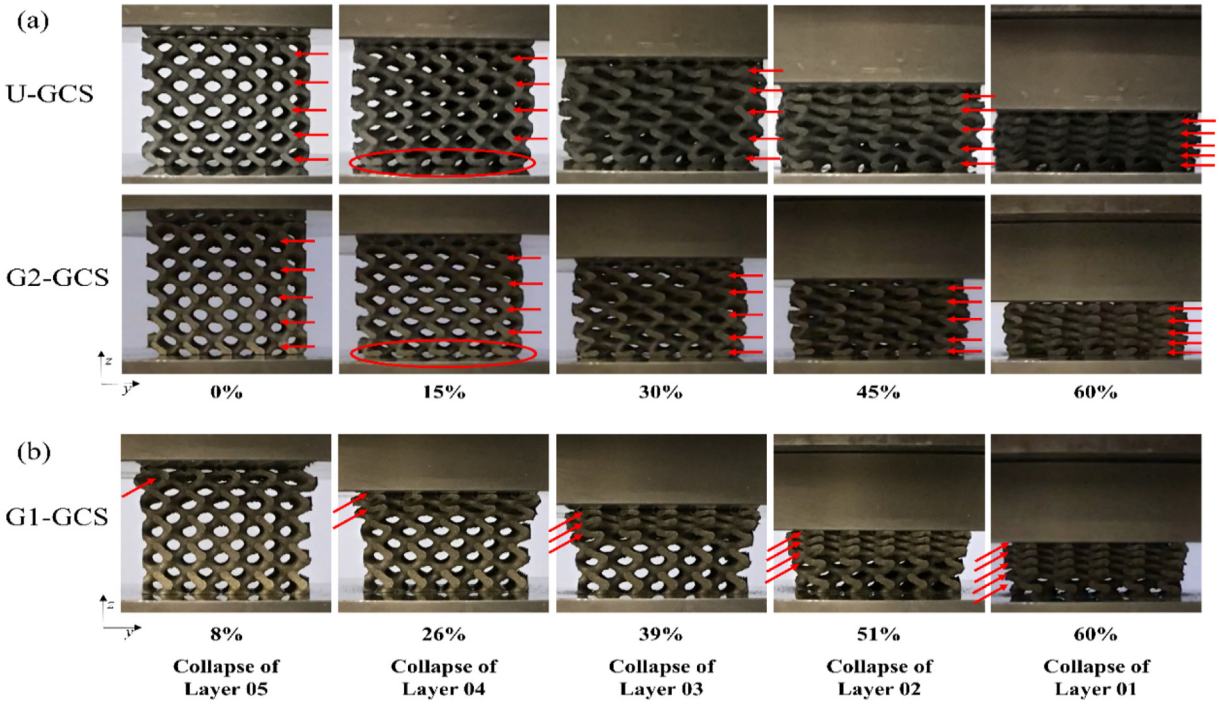

Fig. 5. Deformation stages of U-GCS and G2-GCS in the presence of 0%, 15%, 30%, 45%, and 60% compression strain and layer-by-layer collapses of G1-GCS recorded by the high-speed camera.

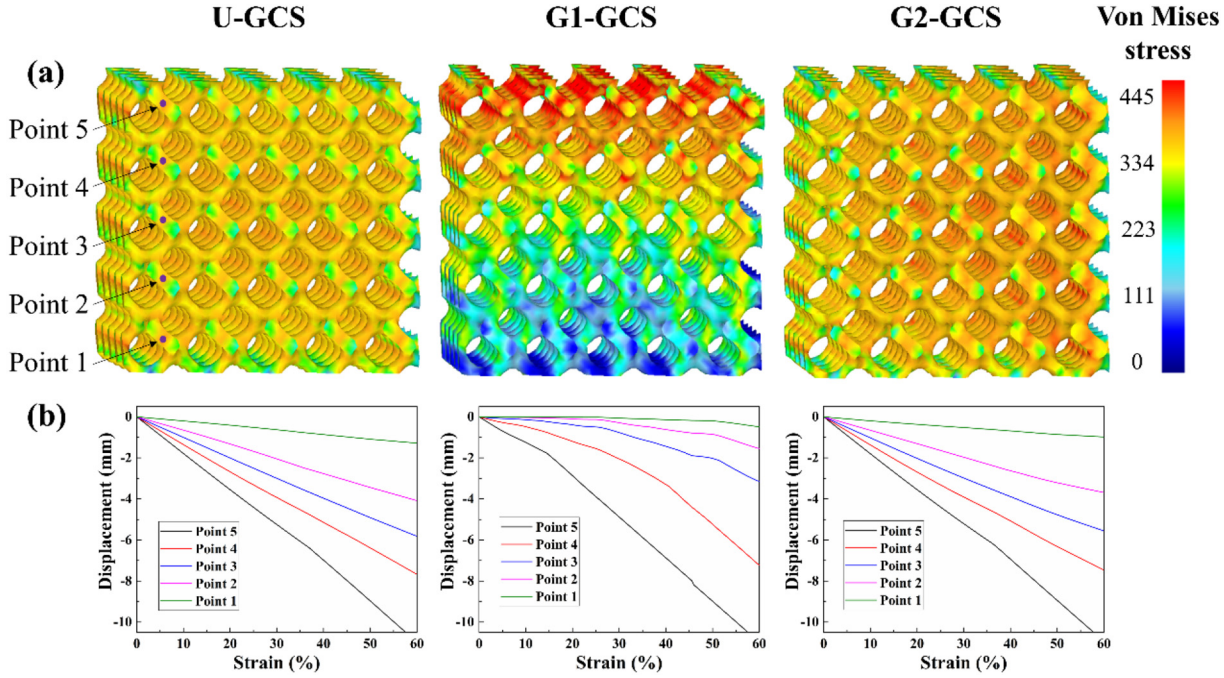

Fig. 7. FE results of the compressive tests: a) Von Mises stress distribution of GCSs at 2% strain, b) the displacement of different points in different layers versus overall strain of GCSs. The position of each point is marked in panel 7(a).

the G1-GCS curves in Fig. 6(a). After each layer collapses, the stress value rises, due to the increase in RD. Fig. 7(a) also shows that the top layer with low RD experiences a high-stress level from the beginning of the compressive testing. For each collapse, the GCS experiences a linear elastic region, a plastic yield region, and a short plastic plateau. The strain interval of each collapse shortens with increasing layer, and it is difficult to determine the collapse of the final layer, as a result of the shorter strain interval.

The layer-by-layer collapse phenomenon was also observed on GCS consisted of other unit cells [15,49]. A series of diamond FGSs with different porosity variation strategies were designed and experimentally tested by Zhang et al. [49], while the compressive properties of functional graded F2BCC lattices were investigated by Al-Saedi et al. [15]. However, the layer-by-layer collapse in [15,49] accompanied with strength lost due to the fracture in cell walls/struts and flake formation of the structures, while in this paper, a stair-stepping plateaus were found, which could be attributed to the ductility of material 316 L stainless steel.

The shorter strain interval for the layer-by-layer collapses in GCS was also documented in [50], but was not thoroughly explained. Firstly, for graded cellular structures with the gradient along the loading direction, the force transmitted to the high-density layer also results in an elastic or plastic deformation, while the layers with lower RDs experience collapse. As these layers collapse, the deformed struts make contact with each other, and the stress level increases gradually due to the increase of the RD of deforming part. Therefore, for layers other than the top layer, the struts also deform prior to the collapsing, as shown in Fig. 7(b). The strain interval of the top layer collapse includes the deformation of all layers, while the strain interval of the bottom layer collapse only includes the deformation of the bottom layer. Furthermore, due to the loss in height from EDM [51], the actual height of the bottom layer is less than others. Consequently, the bottom layer collapse lasted a shorter amount of time and could be obscured by the previous layer.

Meanwhile, beyond the first linear elastic regime, many sub-layer collapses are found in the stress-strain curve between the collapses of layer 5 and layer 4, as shown in Fig. 6(b). Same phenomenon is also seen between the collapses of layer 4 and layer 3 (Fig. 6(c)), but not observed in the later part of stress-strain curves (as shown in Fig. 6(a), between the labels 3-2 and 2-1). The sub-layer collapse can be attributed to the gradient inside of the unit cell. For each unit cell, struts can be segmented into 4 sub-layers along the z coordinate, as shown in Fig. 1(c) and (d). Thus, within one layer, collapsing occurs sequentially from the lowest density sub-layer to the higher density sub-layer. This phenomenon is easy to be ignored, and not been reported in relevant literature [7,15,52]. However, this observation demonstrates the possibility of a more precise control of mechanical properties in G-GCSs by optimizing density distribution in the range of the unit cell. In the later part of stress-strain curves, the sub-layer collapse is not observed, which is mainly due to the shorter strain interval making it harder to distinguish the sub-layer collapse.

3.2.2. Mechanical properties of as-built GCSs under compressive testing

Young's moduli, E_{cel}, plateau stresses, $\sigma_{cel.\ pl}$, and onset strains of densification, ε_{cd}, of GCSs were determined and listed in Table 1. The strain for determining the plateau stress of GCS with uniform topologies along the building direction ranges from 20%–40%, as the plateau regime ends for strain values higher than 40% [40].

The onset of densification of cellular structures is the start point of densification and represents the start of the cell wall/strut interactions with each other. So the point means the end of the plateau region and collapse for uniform cellular structures. However, for G1-GCS, there are several collapses and after each collapse, part of struts interacts with each other, so the whole process includes multi-layer densification, even sub-layer densification. However, an overall densification is

Table 1
Mechanical properties and energy absorption of as-built Gyroid samples under compressive testing.

Properties	U-GCS	G1-GCS	G2-GCS
E_{cel} (MPa)	1097.87 ± 20.85	898.05 ± 13.12	1165.49 ± 11.55
E^* (10^{-3})	5.32 ± 0.10	4.28 ± 0.06	5.55 ± 0.05
$\sigma_{cel.\ pl}$ (MPa)	26.18 ± 0.33	15.82 ± 0.10	27.83 ± 0.01
σ^* (10^{-3})	154.01 ± 1.93	93.08 ± 0.55	163.69 ± 0.08
ε_{cd} (%)	61.23 ± 0.67	62.32 ± 1.00	60.09 ± 0.57
W_v (MJ/m^3)	16.21 ± 0.22	16.60 ± 0.48	16.82 ± 0.18

obtained as the densification of the whole model, and the last onset of densification is obtained for the whole model. In detail, the values ε_{cd} were determined using the energy absorption efficiency method mentioned in Section 1.1. Energy absorption efficiency-strain curves were determined and are presented in Fig. 8 (for each structure, only one sample is shown here). The onset strain values of densification were measured via Eq. (5). The compressive yield strength and elastic modulus of the matrix material 316 L stainless steel are 170 MPa and 210 GPa, respectively [48].

Young's moduli and plastic plateau strength of G2-GCSs are marginally higher than those of U-GCSs by 6.16% and 4.32%, respectively, due to the density gradient perpendicular to the building direction. Although the increase of the mechanical properties of G2-GCS is slight higher in this case (gradient from 20% to 10%), it would be much higher while the gradient is large enough, which will be discussed in Section 3.3.2. Both two structures show high mechanical responses compared to G1-GCS, as the mechanical properties of G1-GCS are determined by iso-stress composite models [53], and will be further discussed in Section 3.3.1.

The relative cellular properties E^* and σ^* can be determined by normalizing E_s and σ_s (from the stress-strain curves) using Young's modulus and the yield stress of the matrix material. Therefore, assuming $m = 2$ and $n = 1.5$ and setting the RD value to 0.15, the Gibson-Ashby coefficients C_1, C_2, and α are determined through Eqs. (1), (2), and (3) and shown in Table 2.

The determined values of C_1 are found to be 0.232, 0.190, and 0.239 for three GCSs, respectively. These values fall within the given range of Gibson and Ashby and are comparable to those found by other researchers. For example, the coefficient C_1 for AlSi10Mg BCC metallic cellular structures and polymeric cellular structures investigated by Maskery et al. were 0.166 and 0.44, respectively [7,50], and C_1 values of 0.17 and 0.19 for 2 types of Ti6Al4V metallic cellular structures were reported by Yan et al. [25]. The calculated values of $\boldsymbol{\alpha}$ for the three types of GCS in this study are 2.635, 2.512 and 2.703, which are similar to the values of 2.449 and 2.87 found in [50].

However, the determined values for parameter C_2, are 2.627, 1.602 and 2.778, which are out of the range given by Gibson and Ashby, and are larger than the values reported by other researchers [7,50]. It is known that values vary from one lattice or foam type to another. For instance, for BCC and BCCz (reinforced variant of BCC) used in [50], the corresponding values of C_2 are 0.202 and 0.285, respectively; while Ahmadi et al. reported the C_2value of 0.35 for Ti6Al4V diamond lattice [16]. The larger C_2 indicates that the GCS possesses a higher strength compared to other strut-based lattice structure, due to the self-supporting property. Our previous work also obtained a relative higher C_2 value of 1.29 for GCS [35]. The difference between the value of C_2 determined here and the value determined in [35] can be attributed to differences in the parameters of the SLM processes.

Table 2
Gibson-Ashby coefficients for GCSs loaded in their building direction.

Coefficients	U-GCS	G1-GCS	G2-GCS
C_1	0.232	0.190	0.247
C_2	2.651	1.602	2.818
α	2.584	2.512	2.660

3.2.3. Energy absorption

The energy absorption capability of cellular structures provides an effective understanding of cellular structures in impact applications [15]. The cumulative energy absorption values per unit volume, W_v, of the cellular structures are determined from Eq. (6) and presented in Fig. 9. The cumulative values of energy absorption up to the onset of densification strain of GCS represent the energy absorption capability which are shown in Table 1.

The curves of the U-GCS and G2-GCS in Fig. 9 are characterized by large linear regions that are directly proportional to the lattice strain, due to the plastic plateau from approximately 5% to 60% strain. After the onset of densification (identified by the vertical and horizontal dashed lines), the curves diverge from their approximately linear behaviour, which can be attributed to the increase of density as well as structural stiffness after the collapses of all layers. As observed previously in the stress-strain curves, Young's moduli and plateau strength of G2-GCSs are both higher than those of U-GCSs due to the density gradient in the layer. Here, it is also readily caught that the energy absorption curves of G2-GCSs are higher than the U-GCSs curves. The total values of cumulative energy absorbed up to densification for G2-GCS and U-GCS are 16.82 ± 0.18 MJ/m^{3}and 16.21 ± 0.22 MJ/m^3, respectively. In contrast to the U-GCS and G2-GCS, the cumulative energy absorption values per unit volume of the G1-GCSs before the onset of densification are roughly proportional to $\varepsilon^{1.55}$. Significantly less energy per unit volume was absorbed during the low strain period for G1-GCSs compared to the structures of U-GCS and G2-GCS without gradient along the loading direction. However, after the successive collapses of the weaker cells, the absorbed energy increases rapidly. At around 62.32 ± 1.00% strain, corresponding to the onset of densification, the energy absorbed by G1-GCS has already overtaken U-GCS with the

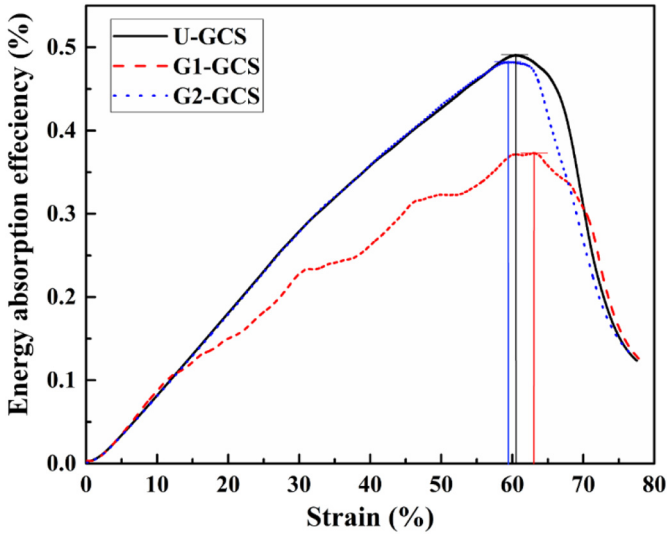

Fig. 8. Efficiency-strain curves and schematic for determining onset strain of GCSs.

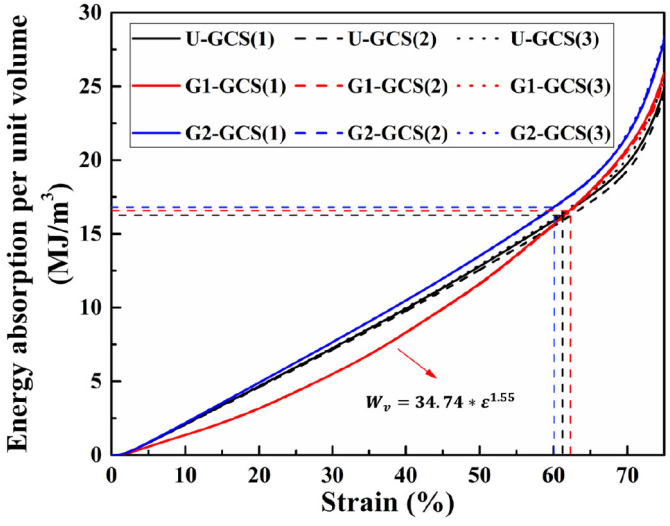

Fig. 9. Energy absorption per unit volume for GCSs under compressive testing. Notations (1), (2), and (3) in the legend correspond to three samples of the same type of GCS.

value of 16.60 ± 0.48 MJ/m^3. The results from Table 1 indicate that the onset strain ε_{cd} of G1-GCS is larger than those of U-GCS and G2-GCS, suggesting that the G1-GSC not only possesses higher energy absorption capability but also provides a large-strain protection before densification, e.g. in crashworthiness application.

3.3. Prediction of the mechanical responses of GCSs

The mechanical response of G-GCSs characterized by Gibson-Ashby models only depends on the equivalent RD of the whole cellular structure. The gradient distribution inside of the cellular structure is not considered in the models, therefore, a precise prediction cannot be obtained from the Gibson-Ashby model. In this study, G-GCSs are treated as a simple series composition of uniform layers with various RD [54]. The RD for each composition is determined as the equivalent RD of the layer. Experimentally determined Young's modulus E_{cel} and plateau stress $\sigma_{cel.\ pl}$ at 15% RD and the values at other RD values predicted from Gibson-Ashby models are shown in Table 3. These values can be used to predict the mechanical properties of a GCS consisting of many layers.

3.3.1. G1-GCSs with a density gradient along the loading direction

For cellular structures with a density gradient along the loading direction, by assuming them as the iso-stress composite models [53], the rule of mixtures (i.e. slab model) [54] can be used when the loading direction is normal to the building layers and described as,

$$\frac{1}{E_{cel}} = \sum_{1}^{n} k_n \frac{1}{E_n} \tag{8}$$

where the subscripts n denotes the layer number, and $\boldsymbol{k_n}$ is the volume percentage of the cubic occupied by the layer with respect to the entire cellular structure, which is designed to be 20% for every layer. However, due to excessive cutting in the EDM removal process [51], the actual total sample height is below 20 mm, therefore, the value of C_n needs to be corrected for each layer. The predicted E_{cel} is 906.54 ± 0.89 MPa with a low percentage deviation of 0.95% compared to the experimental value in Table 1, showing high accuracy.

The yield strength and plateau strength of each layer in G-GCSs are believed to be related with the layer itself and the connection with the neighbouring layer does not significantly affect the strength [54]. Therefore, the plateau strength of each layer in G1-GCS can be considered equivalent to that of U-GCS with the same RD. The predicted and experimental plateau stresses for each layer in G1-GCS are presented in Fig. 10. The results indicate that the experimental values are larger than the predicted values, which is mainly due to the different strain rate of the struts. As shown in Fig. 6(a), the linear elastic regions of structures with graded density along loading direction is shorter than the ones with uniform density, making the strain rate of the struts higher than the uniform ones. It is well known from the material strength models (Johnson-Cook model [55] and Zerilli and Armstrong model [56]) that the yield stress increases as increasing the strain rate of the materials. Mihalikova and Janek [57] also experimentally illustrated the strain rate effect on the strength of the metal material.

Thus, the strength of each layer in G1-GCS is higher than that of uniform structures.

Besides, the prediction for the first layer was closest to its experimentally observed values, with a deviation of 9.9%; and then the deviation shows a rising trend with increasing layer number, which can be explained by the work hardening caused by the continuous deformation before the collapse of this layer.

Table 3
Experimental determined Young's modulus and plateau stress at 15% RD (with *) and values for other RD predicted from the Gibson-Ashby models.

	10%	12.5%	15%	17.5%	20%
E_{cel} (MPa)	487.94	762.41	1093.87*	1494.32	1951.77
$\sigma_{cel.\ pl}$ (MPa)	14.25	19.93	26.18*	32.99	40.31

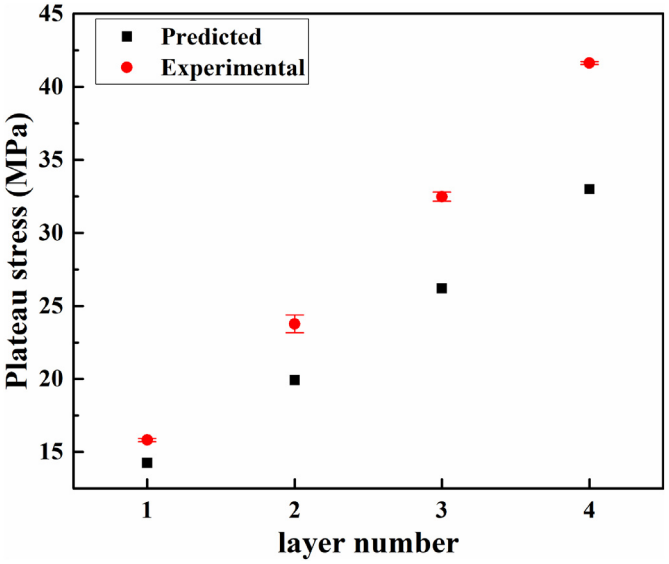

Fig. 10. Predicted and experimental plateau stresses of each layer in G1-GCS.

3.3.2. G2-GCSs with a density gradient perpendicular to the loading direction

For G2-GCS, Young's modulus and plateau stress can be analysed using the Kelvin-Voigt model [58,59], and determined as the weighted average of Young's modulus and plateau stress of all layers. According to this model, Young's modulus and plateau strength of G2-GCS are given respectively by:

$$E_{cel} = \sum_{1}^{n} k_n * E_n \tag{9}$$

$$\sigma_{cel.pl} = \sum_{1}^{n} k_n * \sigma_n \tag{10}$$

By substituting Young's moduli and plateau stresses of different U-GCSs in Table 3, the effective Young's modulus and plateau of the G2-GCSs were calculated. The predicted Young's modulus and plateau stress are 1158.86 MPa and 26.73 MPa, with percentage deviations of 0.57% and 3.95% respectively compared to the experimental values in Table 1.

The higher mechanical responses of G2-GCS compared to U-GCS can be explained as followed. As shown in Eqs. (9) and (10), the mechanical contribution of each layer to the whole structure is linear superposition, while the mechanical increase is non-linear with respect to RD, which can be predicted by Eqs. (1) and (2) with the coefficients in Table 2. As shown in Fig. 11, the Young modulus curves for G2-GCS and U-GCS illustrate the resistance to deformation at different coordinate positions along the Y axis. District I and II correspond to the negative and positive deviations, respectively, for G2-GCS compared to U-GCS. The absolute value of positive deviation is larger than that of negative deviation, resulting in a higher mechanical response of G2-GCS.

However, due to the linear gradient, the average RD of G2-GCS locates at the middle of this model, and the value is equal to that of U-GCS. Therefore, the deviation of two sides in Fig. 11 nearly counteract each other, making the increases of Young's modulus, plateau stress, and absorbed energy only slightly higher. Based on this analysis, a larger or nonlinear gradient in G2-GCS would result in an increase of the difference between absolute values of District I and II larger. As a result,

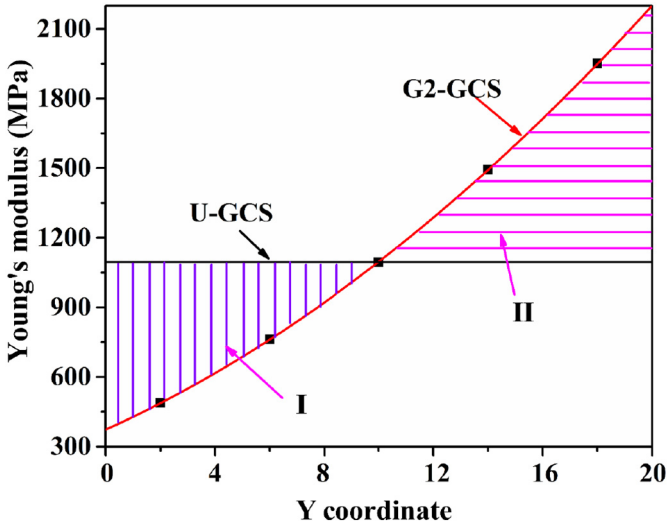

Fig. 11. Comparison of Young's modulus at different coordinate positions along Y axis for U-GCS and G2-GCS.

the deviation between graded GCS and uniform GCS would be much higher. Similar conclusions were drawn by Sun et al. [3] through numerical simulation, in which it was found that the value of gradient exponential parameter has a significant effect on energy absorption capacity of graded foam, and normally the graded structure is generally superior to the uniform structure.

It is worth noting that the empirical values of exponential m and n are used in this study, while researchers treated as varies and making the prediction more accurate [14,25]. Thus the future work includes a range of lattice structures with varying density, which could explicitly determine C_1, C_2, m, n and α for Gyroid cellular structure, and improve the models for assessing the mechanical properties of G-GCSs.

4. Conclusion

In this work, uniform and graded Gyroid cellular structures with different gradient directions were mathematically designed and manufactured by SLM. The mechanical response of these structures under compressive loading was studied. The following conclusions can be made from this study.

a) SLM-fabricated GCS samples agree well with the designed model, which indicates high manufacturability and repeatability of Gyroid cellular structures fabricated by SLM. Bonded powder particles and step-stair effect were observed due to the nature of SLM
b) Experimental compression results indicate that cellular structures with density gradient perpendicular to the loading direction exhibit deformation behaviours similar to the behaviours observed in uniform density structures, and the gradient perpendicular to the loading direction strengthens the cellular structures in terms of Young's modulus, plateau stress, and energy absorption capacity.
c) The collapse process of cellular structures with the gradient parallel to the loading direction exhibits distinctive layer-by-layer collapse characteristic with gradually rising density and compressive stress. Besides, novel sub-layer collapses are found due to the continuous gradient inside the unit cell. The cellular structures with the gradient along the building direction not only possess higher energy absorption capability but also provide a large-strain protection before densification.
d) Coefficients C_1, C_2 and α in the Gibson-Ashby models were determined; the higher value of C_2 indicates that Gyroid cellular structures own larger strength due to their self-supporting property. Iso-stress composite model and Kelvin-Voigt model were introduced to precisely estimate the mechanical properties of G-GCSs with the gradient along different directions, by combining the properties of uniform GCSs.

The findings in this study indicate that the cellular structure with different graded density and gradient direction can achieve different deformation behaviour and mechanical response under compressive testing. The improved mechanical properties make G-GCSs attractive solutions for topology optimization, orthopedics, acoustics, and impact industries. Furthermore, the low deviations in the values predicted by Iso-stress composite model and Kelvin-Voigt model illustrate the possibility and reliability of designing graded cellular structures with specific mechanical requirements. Future work includes a range of lattice structures with varying density, which could explicitly determine C_1, C_2, m, n and α for 316 L Gyroid cellular structure, and improve the models for assessing the mechanical properties of G-GCSs.

Author contributions

L.Y., C.Y. and S.Y. conceived the study. L.Y. and R.M. designed and conducted the experimental work. L.Y. and S.Y. analysed the results. L.Y. wrote the manuscript. C.Y., S.Y., M.F., and Y.S. reviewed the manuscript.

CRediT authorship contribution statement

Lei Yang: Conceptualization, Investigation, Methodology, Data curation, Formal analysis, Visualization, Writing - original draft. **Raya Mertens:** Investigation, Methodology. **Massimiliano Ferrucci:** Writing - review & editing. **Chunze Yan:** Conceptualization, Writing - review & editing. **Yusheng Shi:** Writing - review & editing. **Shoufeng Yang:** Conceptualization, Data curation, Formal analysis, Writing - review & editing.

Acknowledgements

The study was supported by the National Natural Science Foundation of China (Grant No. 51671091), the independent R&D subjects of Huazhong University of Science and Technology (Grant No. 2017JYCXJJ005), China Scholarship Council (No. 201706160036), and the MSCA Individual Fellowship FlexCT project (Grant No. 752672).

References

[1] S. Li, S. Zhao, W. Hou, C. Teng, Y. Hao, Y. Li, R. Yang, R.D.K. Misra, Functionally graded Ti-6Al-4V meshes with high strength and energy absorption, Adv. Eng. Mater. 18 (1) (2016) 34–38.
[2] A. Kumar, K.C. Nune, L.E. Murr, R.D.K. Misra, Biocompatibility and mechanical behaviour of three-dimensional scaffolds for biomedical devices: process-structure-property paradigm, Int. Mater. Rev. 61 (1) (2016) 20–45.
[3] G. Sun, G. Li, S. Hou, S. Zhou, W. Li, Q. Li, Crashworthiness design for functionally graded foam-filled thin-walled structures, Mater. Sci. Eng. A 527 (7–8) (2010) 1911–1919.
[4] L.E. Murr, S.M. Gaytan, F. Medina, H. Lopez, E. Martinez, B.I. Machado, D.H. Hernandez, L. Martinez, M.I. Lopez, R.B. Wicker, J. Bracke, Next-generation biomedical implants using additive manufacturing of complex, cellular and functional mesh arrays, Philos. Trans. R. Soc. London, Ser. A 368 (1917) (2010) 1999–2032.
[5] J. Parthasarathy, B. Starly, S. Raman, A design for the additive manufacture of functionally graded porous structures with tailored mechanical properties for biomedical applications, J. Manuf. Process. 13 (2) (2011) 160–170.
[6] W.-S. Lin, T.L. Starr, B.T. Harris, A. Zandinejad, D. Morton, Additive manufacturing technology (direct metal laser sintering) as a novel approach to fabricate functionally graded titanium implants: preliminary investigation of fabrication parameters, Int. J. Oral Maxillofac. Implants 28 (6) (2013) 1490–1495.
[7] I. Maskery, N.T. Aboulkhair, A.O. Aremu, C.J. Tuck, I.A. Ashcroft, R.D. Wildman, R.J.M. Hague, A mechanical property evaluation of graded density Al-Si10-Mg lattice structures manufactured by selective laser melting, Mater. Sci. Eng. A 670 (2016) 264–274.
[8] J. Banhart, Manufacture, characterisation and application of cellular metals and metal foams, Prog. Mater. Sci. 46 (6) (2001) 559–632.
[9] J. Wang, A. Evans, K. Dharmasena, H. Wadley, On the performance of truss panels with Kagome cores, Int. J. Solids Struct. 40 (25) (2003) 6981–6988.

[10] J. Li, S. Li, C. Van Blitterswijk, K. De Groot, A novel porous Ti6Al4V: characterization and cell attachment, J. Biomed. Mater. Res. A 73 (2) (2005) 223–233.
[11] D.T. Queheillalt, D.D. Hass, D.J. Sypeck, H.N. Wadley, Synthesis of open-cell metal foams by templated directed vapor deposition, J. Mater. Res. 16 (4) (2001) 1028–1036.
[12] F.W. Zok, S.A. Waltner, Z. Wei, H.J. Rathbun, R.M. McMeeking, A.G. Evans, A protocol for characterizing the structural performance of metallic sandwich panels: application to pyramidal truss cores, Int. J. Solids Struct. 41 (22−23) (2004) 6249–6271.
[13] M.R.K. Ravari, S.N. Esfahani, M.T. Andani, M. Kadkhodaei, A. Ghaei, H. Karaca, M. Elahinia, On the effects of geometry, defects, and material asymmetry on the mechanical response of shape memory alloy cellular lattice structures, Smart Mater. Struct. 25 (2) (2016), 025008. .
[14] I. Maskery, A.O. Aremu, M. Simonelli, C. Tuck, R.D. Wildman, I.A. Ashcroft, R.J.M. Hague, Mechanical properties of Ti-6Al-4V selectively laser melted parts with body-centred-cubic lattices of varying cell size, Exp. Mech. 55 (7) (2015) 1261–1272.
[15] D.S.J. Al-Saedi, S.H. Masood, M. Faizan-Ur-Rab, A. Alomarah, P. Ponnusamy, Mechanical properties and energy absorption capability of functionally graded F2BCC lattice fabricated by SLM, Mater. Des. 144 (2018) 32–44.
[16] S.M. Ahmadi, G. Campoli, S. Amin Yavari, B. Sajadi, R. Wauthle, J. Schrooten, H. Weinans, A.A. Zadpoor, Mechanical behavior of regular open-cell porous biomaterials made of diamond lattice unit cells, J. Mech. Behav. Biomed. Mater. 34 (2014) 106–115.
[17] S. Limmahakhun, A. Oloyede, K. Sitthiseripratip, Y. Xiao, C. Yan, Stiffness and strength tailoring of cobalt chromium graded cellular structures for stress-shielding reduction, Mater. Des. 114 (2017) 633–641.
[18] M. Dumas, P. Terriault, V. Brailovski, Modelling and characterization of a porosity graded lattice structure for additively manufactured biomaterials, Mater. Des. 121 (2017) 383–392.
[19] X.Y. Cheng, S.J. Li, L.E. Murr, Z.B. Zhang, Y.L. Hao, R. Yang, F. Medina, R.B. Wicker, Compression deformation behavior of Ti-6Al-4V alloy with cellular structures fabricated by electron beam melting, J. Mech. Behav. Biomed. Mater. 16 (2012) 153–162.
[20] O. Cansizoglu, O. Harrysson, D. Cormier, H. West, T. Mahale, Properties of Ti–6Al–4V non-stochastic lattice structures fabricated via electron beam melting, Mater. Sci. Eng. A 492 (1–2) (2008) 468–474.
[21] M. Mazur, M. Leary, S. Sun, M. Vcelka, D. Shidid, M. Brandt, Deformation and failure behaviour of Ti-6Al-4V lattice structures manufactured by selective laser melting (SLM), Int. J. Adv. Manuf. Technol. 84 (5) (2016) 1391–1411.
[22] M. Smith, Z. Guan, W.J. Cantwell, Finite element modelling of the compressive response of lattice structures manufactured using the selective laser melting technique, Int. J. Mech. Sci. 67 (2013) 28–41.
[23] S. Rajagopalan, R.A. Robb, Schwarz meets Schwann: design and fabrication of biomorphic and durataxic tissue engineering scaffolds, Med. Image Anal. 10 (5) (2006) 693–712.
[24] C. Yan, L. Hao, A. Hussein, S.L. Bubb, P. Young, D. Raymont, Evaluation of light-weight AlSi10Mg periodic cellular lattice structures fabricated via direct metal laser sintering, J. Mater. Process. Technol. 214 (4) (2014) 856–864.
[25] C. Yan, L. Hao, A. Hussein, P. Young, Ti-6Al-4V triply periodic minimal surface structures for bone implants fabricated via selective laser melting, J. Mech. Behav. Biomed. Mater. 51 (2015) 61–73.
[26] L. Yang, C. Yan, Y. Shi, Fracture Mechanism Analysis of Schoen gyroid Cellular Structures Manufactured by Selective Laser Melting, Solid Freeform Fabrication Symposium, 2017 2319–2325.
[27] L. Hao, D. Raymont, C. Yan, A. Hussein, P. Young, Design and additive manufacturing of cellular lattice structures, The International Conference on Advanced Research in Virtual and Rapid Prototyping (VRAP), Taylor & Francis Group, Leiria 2011, pp. 249–254.
[28] A. Yanez, A. Herrera, O. Martel, D. Monopoli, H. Afonso, Compressive behaviour of gyroid lattice structures for human cancellous bone implant applications, Mater. Sci. Eng. C 68 (2016) 445–448.
[29] I. Maskery, N.T. Aboulkhair, A.O. Aremu, C.J. Tuck, I.A. Ashcroft, Compressive failure modes and energy absorption in additively manufactured double gyroid lattices, Addit. Manuf. 16 (2017) 24–29.
[30] S. Khaderi, V. Deshpande, N. Fleck, The stiffness and strength of the gyroid lattice, Int. J. Solids Struct. 51 (23–24) (2014) 3866–3877.
[31] M.R. Scherer, L. Li, P.M. Cunha, O.A. Scherman, U. Steiner, Enhanced electrochromism in gyroid-structured vanadium pentoxide, Adv. Mater. 24 (9) (2012) 1217–1221.
[32] V. Luzzati, P. Spegt, Polymorphism of lipids, Nature 215 (5102) (1967) 701–704.
[33] V. Luzzati, A. Tardieu, T. Gulik-Krzywicki, E. Rivas, F. Reiss-Husson, Structure of the cubic phases of lipid–water systems, Nature 220 (5166) (1968) 485–488.
[34] C. Yan, L. Hao, A. Hussein, Q. Wei, Y. Shi, Microstructural and surface modifications and hydroxyapatite coating of Ti-6Al-4V triply periodic minimal surface lattices fabricated by selective laser melting, Mater. Sci. Eng. C 75 (2017) 1515–1524.
[35] C. Yan, L. Hao, A. Hussein, P. Young, D. Raymont, Advanced lightweight 316L stainless steel cellular lattice structures fabricated via selective laser melting, Mater. Des. 55 (2014) 533–541.
[36] L. Yang, C. Yan, C. Han, P. Chen, S. Yang, Y. Shi, Mechanical response of a triply periodic minimal surface cellular structures manufactured by selective laser melting, Int. J. Mech. Sci. 148 (2018) 149–157.
[37] L. Yang, C. Yan, H. Fan, Z. Li, C. Cai, P. Chen, Y. Shi, S. Yang, Investigation on the orientation dependence of elastic response in Gyroid cellular structures, J. Mech. Behav. Biomed. Mater. 90 (2019) 73–85.
[38] L.J. Gibson, M.F. Ashby, Cellular Solids: Structure and Properties, Cambridge University Press, Cambridge; New York, 1997.
[39] Q.M. Li, I. Magkiriadis, J.J. Harrigan, Compressive strain at the onset of densification of cellular solids, J. Cell. Plast. 42 (5) (2016) 371–392.
[40] I. Standard, ISO 13314, (E)(2011) Mechanical Testing of Metals—Ductility Testing—Compression Test for Porous and Cellular Metals, Ref Number ISO 13314(13314), 2011 1–7.
[41] M. Avalle, G. Belingardi, R. Montanini, Characterization of polymeric structural foams under compressive impact loading by means of energy-absorption diagram, Int. J. Impact Eng. 25 (5) (2001) 455–472.
[42] M.R.J. Scherer, Double-Gyroid-Structured Functional Materials: Synthesis and Applications, Springer Science & Business Media, Switerland, 2013.
[43] M. Simonelli, Y.Y. Tse, C. Tuck, Effect of the build orientation on the mechanical properties and fracture modes of SLM Ti–6Al–4V, Mater. Sci. Eng. A 616 (2014) 1–11.
[44] T. DEFORM, 3D Version 6.1 (sp1) User's Manual, Scientific Forming Technologies Corporation, Columbus OH, 2006.
[45] A. Hussein, L. Hao, C. Yan, R. Everson, P. Young, Advanced lattice support structures for metal additive manufacturing, J. Mater. Process. Technol. 213 (7) (2013) 1019–1026.
[46] A. Yánez, A. Cuadrado, O. Martel, H. Afonso, D. Monopoli, Gyroid porous titanium structures: a versatile solution to be used as scaffolds in bone defect reconstruction, Mater. Des. 140 (2018) 21–29.
[47] K. Saeidi, X. Gao, Y. Zhong, Z.J. Shen, Hardened austenite steel with columnar subgrain structure formed by laser melting, Mater. Sci. Eng. A 625 (2015) 221–229.
[48] T. Tancogne-Dejean, A.B. Spierings, D. Mohr, Additively-manufactured metallic micro-lattice materials for high specific energy absorption under static and dynamic loading, Acta Mater. 116 (2016) 14–28.
[49] X.-Y. Zhang, G. Fang, L.-L. Xing, W. Liu, J. Zhou, Effect of porosity variation strategy on the performance of functionally graded Ti-6Al-4V scaffolds for bone tissue engineering, Mater. Des. 157 (2018) 523–538.
[50] I. Maskery, A. Hussey, A. Panesar, A. Aremu, C. Tuck, I. Ashcroft, R. Hague, An investigation into reinforced and functionally graded lattice structures, J. Cell. Plast. 53 (2) (2017) 151–165.
[51] P. Mercelis, J.-P. Kruth, Residual stresses in selective laser sintering and selective laser melting, Rapid Prototyp. J. 12 (5) (2006) 254–265.
[52] C. Han, Y. Li, Q. Wang, S. Wen, Q. Wei, C. Yan, L. Hao, J. Liu, Y. Shi, Continuous functionally graded porous titanium scaffolds manufactured by selective laser melting for bone implants, J. Mech. Behav. Biomed. Mater. 80 (2018) 119–127.
[53] A.H. Brothers, D.C. Dunand, Mechanical properties of a density-graded replicated aluminum foam, Mater. Sci. Eng. A 489 (1–2) (2008) 439–443.
[54] W. van Grunsven, E. Hernandez-Nava, G. Reilly, R. Goodall, Fabrication and mechanical characterisation of titanium lattices with graded porosity, Metals 4 (3) (2014) 401–409.
[55] G.R. Johnson, W.H. Cook, Fracture characteristics of three metals subjected to various strains, strain rates, temperatures and pressures, Eng. Fract. Mech. 21 (1) (1985) 31–48.
[56] F.J. Zerilli, R.W. Armstrong, Dislocation-mechanics-based constitutive relations for material dynamics calculations, J. Appl. Phys. 61 (5) (1987) 1816–1825.
[57] M. Mihalikova, J. Janek, Influence of the loading and strain rates on the strength properties and formability of higher-strength sheet, Meta 46 (2) (2007) 107–110.
[58] L.B. Eldred, W.P. Baker, A.N. Palazotto, Kelvin-Voigt versus fractional derivative model as constitutive relations for viscoelastic materials, AIAA J. 33 (3) (1995) 547–550.
[59] S. Suresh, A. Mortensen, Fundamentals of Functionally Graded Materials, The Institut of Materials, London, 1998.